VOLUME: 9 | ISSUE: 2 | 2025 | June

Free vibration of the FG-GPLRC plates resting on an elastic foundation using the moving Kriging meshfree method

Le Thanh Dat[1],*Pham Tan Hung*[2,*]

[1]Faculty of Mechanical Engineering, Ho Chi Minh City University of Technology and Education, Ho Chi Minh City, Vietnam.
[2]Faculty of Civil Engineering, Ho Chi Minh City University of Technology and Education, Ho Chi Minh City, Vietnam.

*Corresponding Author: Pham Tan Hung (Email: hungpht@hcmute.edu.vn)
(Received: 18-May-2025; accepted: 26-June-2025; published: 30-June-2025)
http://dx.doi.org/10.55579/jaec.202592.500

Abstract. *The paper's main purpose is to analyze the free vibration of graphene platelet-reinforced functionally graded metal foam plates using the C0-type higher-order shear deformation theory (C0-HSDT) with seven variables and the moving Kriging meshfree method (MKMM). Various types of porosity and graphene platelets distributions through the plate's thickness are investigated in this study. Material properties of metal foam plates reinforced with graphene platelets are described using the Halpin-Tsai model. By applying Hamilton's principle alongside the C0-HSDT, the governing equation for free vibration in functionally graded metal foam plate reinforced with graphene platelets is formulated and solved by the moving Kriging meshfree method. The accuracy of the computational model is verified by comparing the vibrational frequencies calculated in this paper with available results from the literature. Following this, the influences of porosity distributions, GPLs distributions, porosity coefficients, GPLs volume fraction, and geometric parameters on vibrational characteristics are examined, thereby contributing to the development of lightweight structures, advanced materials, and structural optimization for specific applications.*

Key Words**:** *Functionally graded metal foam plate, graphene platelets, free vibration, C0-type higher-order shear deformation theory, moving Kriging meshfree method.*

1. Introduction

Functionally graded porous (FGP) structures are artificial materials containing internal pores with material properties that vary continuously according to a predetermined distribution law. By controlling the porosity distribution, it is possible to enhance both the mechanical strength and overall performance of the material. Interestingly, FGP structures can be naturally observed in biological systems, such as the bones of humans and animals. Internal pores significantly reduce structural components' mass and stiffness while improving damping capacity, thermal insulation, and maintaining sufficient mechanical strength [1,2]. On the other hand, graphene platelets (GPLs) are two-dimensional materials made of carbon atoms arranged in a periodic hexagonal mesh through sp^2 hybridization, forming a honeycomb structure. Essentially, graphite—the material used in pencils—consists of stacked graphene layers. However, individual GPLs possess remarkable properties, including exceptional electrical and thermal conductivity, high strength, superior elasticity, low density, extreme thinness, and optical transparency. These outstanding characteristics have attracted extensive research interest, leading to their application in numerous advanced engineering and technology fields [3–8].

In summary, both FGP structures and GPLs exhibit superior mechanical properties. When combined, as in the case of metal foam plates reinforced with graphene platelets, the resulting plate-shell or beam structures can achieve significantly improved mechanical strength, stability, and functional performance. Presently, considerable research has focused explicitly on FGP structures reinforced with GPLs. Mohd *et al.* [9] used the C0-HSDT and finite element method (FEM) to investigate the influence of GPL reinforcement on the stiffness and vibration behavior of FGP-GPL plates. Zanjanchi *et al.* [10] examined the nonlinear vibration and stability behaviors of FGP-GPL plates utilizing the first-order shear deformation theory (FSDT) and the Galerkin method (GM). Guo *et al.* [11] developed a nonlinear vibrational model for FG piezoelectric with GPLRC based on the Halpin–Tsai model, FSDT, and isogeometric approach (IGA). In addition, the vibration and buckling behavior of carbon nanotubes reinforced composite plates are examined by Singh *et al.* [12] based on the non-polynomial shear deformation theory and IGA. Whereas Kiran *et al.* [13] investigated the buckling behavior of cracked isotropic and orthotropic structures using meshfree method based on IGA and the reproducing kernel particle method (RKPM). Further studies include Mohd *et al.* [14], who examined the effects of temperature changes on the free vibration of FGP-GPL arches using HSDT, the Halpin–Tsai model, Voigt's rule of mixtures, and FEM. Chang *et al.* [15] investigated the buckling and post-buckling of the sandwich plates with FGP-GPL core based on the refined shell theory, von Kármán theory, and IGA. Li *et al.* [16] explored the stability of the FGP-GPL arches using the Halpin–Tsai model, Karman's theory, and analytical approach. Khayat *et al.* [17] analyzed the free vibration of truncated conical FGP-GPL shells using the HSDT, Sanders's theory, and the Fourier differential quadrature (FDQ) method. Lu *et al.* [18] studied the dynamic behavior of FGP-GPL spherical shells using FSDT and analytical method. Other related works include Wei *et al.* [19], who determined critical buckling loads in FGP-GPL plates using the Halpin–Tsai model, HSDT, and generalized differential quadrature (GDQ) method. Ye *et al.* [20] examined the forced vibration of FGP-GPL cylindrical shells via Donnell's shell theory and FDQ. Zhao *et al.* [21] analyzed the free vibration of the FGP-GPL doubly curved panels based on FSDT, while Song *et al.* [22] examined the nonlinear vibration and chaotic dynamic behavior of rotating FGP-GPL plates employing the HSDT and GM. Teng *et al.* [23] studied the nonlinear vibration of the FGP-GPL plates using the Kármán theory and GM. Additionally, Pan *et al.* [24] conducted a free vibration approach of the FGP-GPL plates employing the Halpin–Tsai model and GDQ, while Cho *et al.* [25] evaluated the vibrational behavior of the FGP-GPL cylindrical shells using the FSDT and MITC3+ shell element method.

Developed by Gu [26], the moving Kriging meshfree method (MKMM) has been extensively applied to the analysis of plate, shell, and beam structures. Unlike the FEM, this numerical technique does not require discretizing the computational domain into complex meshes. Instead, it discretizes the problem domain into a set of scattered nodes, thereby simplifying the preprocessing stage and facilitating computations involving complex geometries. The MKMM has been widely used in various engineering applications, such as vibration analysis, static and dynamic analysis, and fracture mechanics. For instance, Thai *et al.* [27] employed this method combined with a two-variable refined plate theory to investigate the free vibration of isotropic plates. Bui *et al.* [28] adopted a meshfree approach based on the GM and MK interpolation functions to study the free vibration behavior of two-dimensional structures. Similarly, Peng *et al.* [29] utilized the MKMM to analyze both the static and dynamic responses of the FGM plates. Hung *et al.* [30] used the MKMM to analyze the free vibration of FGP-GPL magneto-electro-elastic plates. Bui *et al.* [31] analyzed the free vibration of a Kirchhoff plate utilizing the MKMM. Thai *et al.* [32] employed the MKMM for the static, dynamic, and bending analyses of isotropic and FGM sandwich plates.

To the best of the authors' knowledge, the novelty and research gap lie in the fact that no prior work has applied the C0-HSDT and MKMM to analyze the linear free vibration of FGP-GPL plates resting on a Winkler-Pasternak foundation. Therefore, this study introduces an alternative and efficient numerical approach for investigating the free vibration behavior of functionally graded porous plates reinforced with graphene platelets based on the C0-HSDT with seven variables and MKMM. Additionally, the effects of porosity coefficients, porosity and GPL distributions, GPL weight fraction, and plate geometry on the vibration behavior of the FGP-GPL plate are investigated.

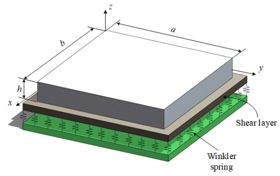

(a) FGP-GPL rectangular plates

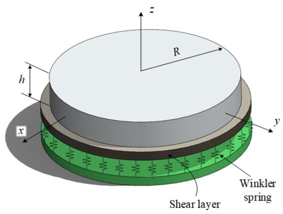

(b) FGP-GPL circular plates

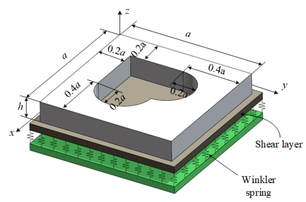

(c) FGP-GPL square plates with a cutout heart

Fig. 1: Geometry of the FGP-GPL plates.

2. The fundamental equations

2.1. Material properties

In this paper, we consider FGP-GPL rectangular plates, circular plates and square plates with a cutout heart. Their dimensions are shown in Figure 1. Where $a, b, andh$ denote the length, width, and thickness of the rectangular plate, respectively. Whereas R denotes the radius of the circular plate. The pores of metal foam plates vary through the thickness direction, which is also known as porosity distribution. Three types of porosity distributions are considered: symmetric distributions (P-I and P-II) and uniform distribution (P-III). The configurations of these distributions are illustrated in Figure 2. The mechanical properties of the FGP plate with different porous distributions are represented as follows [33]

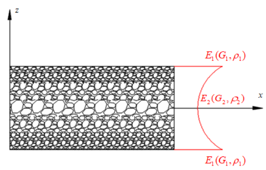

(a) Symmetric I (P-I)

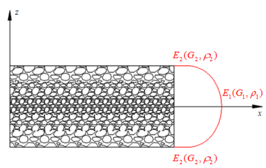

(b) Symmetric II (P-II)

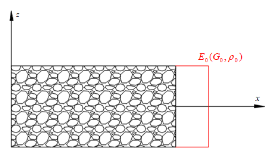

(c) Uniform (P-III)

Fig. 2: Porosity distributions.

$$\mathrm{P-I}:\begin{cases} E(z)=E_1(1-e_0\cos\kappa) \\ G(z)=G_1(1-e_0\cos\kappa) \\ \rho(z)=\rho_1(1-e_m\cos\kappa) \end{cases} \tag{1}$$

$$\mathrm{P-II}:\begin{cases} E(z)=E_1[1-e_0^*(1-\cos\kappa)] \\ G(z)=G_1[1-e_0^*(1-\cos\kappa)] \\ \rho(z)=\rho_1[1-e_m^*(1-\cos\kappa)] \end{cases} \tag{2}$$

$$\mathrm{P-III}:\begin{cases} E(z)=E_1 s_0 \\ G(z)=G_1 s_0 \\ \rho(z)=\rho_1 s_m \end{cases} \tag{3}$$

where $\kappa = \frac{\pi z}{h}$; $E(z), G(z)$ and $\rho(z)$ represent the elastic modulus, shear modulus and mass density of the FGP plate, respectively; E_1, G_1 and ρ_1 denote the maximum elastic modulus, the maximum shear modulus and the maximum mass density, respectively; e_0 and e_0^* represent the porosity coefficient of P-I and P-II (with $0 < e_0(e_0^*) < 1$); s_0 denotes the P-III porous coefficient. Conversely, e_m, e_m^*, and s_m represent the mass porosity coefficient associated with P-I, P-II, and P-III, respectively.

The porosity coefficient is defined as follows:

$$e_0 = 1 - \frac{E_2}{E_1} = 1 - \frac{G_2}{G_1} \tag{4}$$

where E_2 and G_2 indicate the minimum elastic and shear modulus, respectively.

Based on the structure properties of the FGP plate with an open-wall, the relationship between mass density and elastic modulus is formulated by the following expression [34, 35]:

$$\frac{\rho(z)}{\rho_1} = \sqrt{\frac{E(z)}{E_1}} \tag{5}$$

Replacing Eq. 5 into Eqs. 1,2, and 3, we have:

$$\begin{aligned} &1 - e_m \cos\left(\tfrac{\pi z}{h}\right) = \sqrt{1 - e_0 \cos\left(\tfrac{\pi z}{h}\right)} \\ &1 - e_m^* \left[1 - \cos\left(\tfrac{\pi z}{h}\right)\right] = \sqrt{1 - e_0^* \left[1 - \cos\left(\tfrac{\pi z}{h}\right)\right]} \\ &s_m = \sqrt{s_0} \end{aligned} \tag{6}$$

To ensure a fair comparison, the overall mass of the FGP plates with different porosity distributions must be equal and is given by the following formula

$$\begin{cases} \int_{-\frac{h}{2}}^{\frac{h}{2}} \sqrt{1 - e_0^* \left[1 - \cos(\kappa)\right]} dz = \int_{-\frac{h}{2}}^{\frac{h}{2}} \sqrt{1 - e_0 \cos(\kappa)} dz \\ \int_{-\frac{h}{2}}^{\frac{h}{2}} \sqrt{s_0} dz = \int_{-\frac{h}{2}}^{\frac{h}{2}} \sqrt{1 - e_0 \cos(\kappa)} dz \end{cases} \tag{7}$$

Based on Eq. 7, the relationship between e_0, e_0^* and s_0 is given and tabulated in Table 1. As seen in Table 1, when substituting $e_0 = 0.6$, the value of e_0^* converges to its limit. Therefore, the coefficient of e_0 lies within the range of 0.1 to 0.6.

Using the Halpin-Tsai model [36, 37] for the FGP-GPL plate, the Young's modulus E_1 in Eqs. 1-3 is calculated as follows

Tab. 1: The relationship among porosity coefficients [30].

e_0	e_0^*	s_0
0.1	0.1738	0.9361
0.2	0.3442	0.8716
0.3	0.5103	0.8064
0.4	0.6708	0.7404
0.5	0.8231	0.6733
0.6	0.9612	0.6047

$$E_1 = \frac{E_m}{8}\left[3\frac{1+\zeta_L \eta_L V_{GPL}(z)}{1-\eta_L V_{GPL}(z)} + 5\frac{1+\zeta_W \eta_W V_{GPL}(z)}{1-\eta_W V_{GPL}(z)}\right] \tag{8}$$

$$\begin{aligned} \zeta_L &= \frac{2l_{GPL}}{t_{GPL}}; \eta_L = \frac{E_{GPL} - E_m}{E_{GPL} + E_m \zeta_L}; \\ \zeta_W &= \frac{2w_{GPL}}{t_{GPL}}; \eta_W = \frac{E_{GPL} - E_m}{E_{GPL} + E_m \zeta_W} \end{aligned} \tag{9}$$

where, E_m uses to express the elastic modulus of the matrix; L_{GPL} and t_{GPL} represent the average length and width of GPL, respectively; E_{GPL} denotes the GPLs elastic modulus; w_{GPL} is the average thickness of GPL. Finally, $V_{GPL}(Z)$ is the volume fraction of the GPL. In this work, the GPLs are dispersed through the plate's thickness in multiple forms, as depicted in Figure 3. The expression of GPL volume fraction $V_{GPL}(Z)$ for different GPL distributions is formulated as follows [30]:

$$V_{GPL}(z) = \begin{cases} V_{iA}\left[1 - \cos(\kappa)\right] & \mathrm{GPL-A} \\ V_{iB} \cos(\kappa) & \mathrm{GPL-B} \\ V_{iC} & \mathrm{GPL-C} \end{cases} \tag{10}$$

where, V_{iA}, V_{iB} and V_{iC} represent the highest GPL volume fractions of type A, B, and C inside the FGP-GPL plate. Meanwhile, $i = 1, 2$ and 3, respectively, denote the porous distribution of P-I, P-II and P-III.

The mass density ρ_1 and Poisson coefficient of the FGP-GPL plate are defined as follows [38]

$$\begin{cases} \rho_1 = \rho_m V_m + \rho_{GPL} V_{GPL} \\ \nu_1 = \nu_m V_m + \nu_{GPL} V_{GPL} \\ V_m = 1 - V_{GPL} \end{cases} \tag{11}$$

where, ρ_m and ρ_{GPL} are the mass density of the matrix and GPLs; ν_m and ν_{GPL} represent the Poisson coefficient of FGP and GPLs, respectively. The volume fraction V_{GPL} and weight

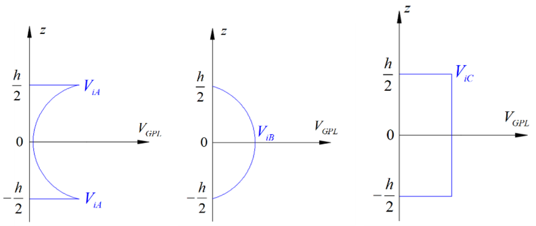

(a) GPL-A (b) GPL-B (c) GPL-C

Fig. 3: GPLs distributions of the FGP-GPL plate.

fraction W_{GPL} of GPLs are related by the following expression [30]

$$V_{GPL} = \frac{W_{GPL}\rho_m}{W_{GPL}\rho_m + \rho_{GPL}\left(1 - W_{GPL}\right)} \tag{12}$$

Based on Eqs. 10, 12, and mass density fraction $\frac{\rho(z)}{\rho_1}$, the maximum volume fraction V_{iA}, V_{iB}, and V_{iC} are determined as follows:

$$\frac{W_{GPL}\rho_m}{W_{GPL}\rho_m + \rho_{GPL}(1 - W_{GPL})} \int_{-\frac{h}{2}}^{\frac{h}{2}} \frac{\rho(z)}{\rho_1} dz = \begin{cases} V_{iA} \int_{-\frac{h}{2}}^{\frac{h}{2}} \left[1 - \cos(\kappa)\right] \frac{\rho(z)}{\rho_1} dz \\ V_{iB} \int_{-\frac{h}{2}}^{\frac{h}{2}} \cos(\kappa) \frac{\rho(z)}{\rho_1} dz \\ V_{iC} \int_{-\frac{h}{2}}^{\frac{h}{2}} \frac{\rho(z)}{\rho_1} dz \end{cases} \tag{13}$$

2.2. The governing equations

As per the C0-HSDT [38], the displacement field at a given point on the plate is defined as follows

$$\begin{cases} u(x,y,z) = u_0(x,y) - z\beta_x(x,y) + f(z)\theta_x(x,y) \\ v(x,y,z) = v_0(x,y) - z\beta_y(x,y) + f(z)\theta_y(x,y) \\ w(x,y,z) = w_0(x,y) \end{cases} \tag{14}$$

with $f(z) = z - \frac{4z^3}{3h^2}$; u_0 and v_0 represent the displacements of any point of the middle plane in the x and y directions, respectively; w_0 denotes the transverse displacement of the point in the middle plane; θ_x and θ_y are the rotation angles of the middle plane around the y and x axis, respectively; $\beta_x = w_{0,x}$ and $\beta_y = w_{0,y}$. The index "," represents the partial derivative.

The matrix form of Eq. 14 is as follows

$$\mathbf{u} = \mathbf{u}_0 + z\mathbf{u}_1 + f(z)\mathbf{u}_2 \tag{15}$$

where

$$\mathbf{u}_0 = \begin{Bmatrix} u_0 \\ v_0 \\ w_0 \end{Bmatrix}; \mathbf{u}_1 = \begin{Bmatrix} -\beta_x \\ -\beta_y \\ 0 \end{Bmatrix}; \mathbf{u}_2 = \begin{Bmatrix} \theta_x \\ \theta_y \\ 0 \end{Bmatrix}$$

The strain tensor is determined by the displacement u in Eq. 15, as follows

$$\boldsymbol{\varepsilon}_b = \boldsymbol{\varepsilon}_{b0} + z\boldsymbol{\varepsilon}_{b1} + f(z)\boldsymbol{\varepsilon}_{b2};\ \boldsymbol{\varepsilon}_s = \boldsymbol{\varepsilon}_{s0} + f'(z)\boldsymbol{\varepsilon}_{s1} \tag{16}$$

where

$$\boldsymbol{\varepsilon}_b = \begin{Bmatrix} \varepsilon_x \\ \varepsilon_y \\ \gamma_{xy} \end{Bmatrix}; \boldsymbol{\varepsilon}_s = \begin{Bmatrix} \gamma_{xz} \\ \gamma_{yz} \end{Bmatrix}; \boldsymbol{\varepsilon}_{b1} = \begin{Bmatrix} -\beta_{x,x} \\ -\beta_{y,y} \\ -\beta_{x,y} - \beta_{y,x} \end{Bmatrix};$$
$$\boldsymbol{\varepsilon}_{b0} = \begin{Bmatrix} u_{0,x} \\ v_{0,y} \\ u_{0,y} + v_{0,x} \end{Bmatrix}; \boldsymbol{\varepsilon}_{b2} = \begin{Bmatrix} \theta_{x,x} \\ \theta_{y,y} \\ \theta_{x,y} + \theta_{y,x} \end{Bmatrix};$$
$$\boldsymbol{\varepsilon}_{s0} = \begin{Bmatrix} -\beta_x + w_{0,x} \\ -\beta_y + w_{0,y} \end{Bmatrix}; \boldsymbol{\varepsilon}_{s1} = \begin{Bmatrix} \theta_x \\ \theta_y \end{Bmatrix}. \tag{17}$$

The constitutive relation is formulated as follows

$$\begin{cases} \boldsymbol{\sigma}_b = \mathbf{C}_b\boldsymbol{\varepsilon}_b \\ \boldsymbol{\sigma}_s = \mathbf{C}_s\boldsymbol{\varepsilon}_s \end{cases} \tag{18}$$

with

$$\boldsymbol{\sigma}_b = \begin{Bmatrix} \sigma_x \\ \sigma_y \\ \tau_{xy} \end{Bmatrix}; \mathbf{C}_b \begin{bmatrix} C_{11} & C_{12} & 0 \\ C_{12} & C_{22} & 0 \\ 0 & 0 & C_{66} \end{bmatrix};$$
$$\boldsymbol{\sigma}_s = \begin{Bmatrix} \tau_{xz} \\ \tau_{yz} \end{Bmatrix}; \mathbf{C}_s = \begin{bmatrix} C_{55} & 0 \\ 0 & C_{44} \end{bmatrix}$$

in which $\sigma_x, \sigma_y, \tau_{xy}, \tau_{xz}, \tau_{yz}$ indicate the stress component; C_{ij} express the elastic coefficients, which are calculated as follows

$$\begin{aligned} C_{11} = C_{22} = \frac{E}{1-\nu^2}; C_{12} = \frac{E\nu}{1-\nu^2}; \\ C_{44} = C_{55} = C_{66} = G = \frac{E}{2(1+v)} \end{aligned} \tag{19}$$

According to Hamilton's principle, the governing equation of the FGP-GPL plates is given by

$$\int_0^t (\delta\Pi - \delta T - \delta W)dt = 0 \tag{20}$$

where $\delta\Pi$ represents the variation of elastic potential energy, δT refers to the variation in kinetic energy, while δW refers to the variation in work performed by the elastic foundation.

The variation of elastic potential energy variation is expressed as follows

$$\delta\Pi = \int\limits_V \delta\boldsymbol{\varepsilon}_b^T \boldsymbol{\sigma}_b dV + \int\limits_V \delta\boldsymbol{\varepsilon}_s^T \boldsymbol{\sigma}_s dV \tag{21}$$

The kinetic energy variation is presented as follows

$$\delta T = -\int_\Omega \delta\bar{\mathbf{u}}^T \mathbf{I}_m \ddot{\bar{\mathbf{u}}} d\Omega \tag{22}$$

where

$$\bar{\mathbf{u}} = \begin{Bmatrix} \mathbf{u}_0 \\ \mathbf{u}_1 \\ \mathbf{u}_2 \end{Bmatrix}; \ \mathbf{I}_m = \begin{bmatrix} \mathbf{I}_0 & \mathbf{0} & \mathbf{0} \\ \mathbf{0} & \mathbf{I}_0 & \mathbf{0} \\ \mathbf{0} & \mathbf{0} & \mathbf{I}_0 \end{bmatrix}; \ \mathbf{I}_0 = \begin{bmatrix} I_1 & I_2 & I_4 \\ I_2 & I_3 & I_5 \\ I_4 & I_5 & I_6 \end{bmatrix};$$
$$(I_1, I_2, I_3, I_4, I_5, I_6) = \int_{-h/2}^{h/2} \rho(z)\left(1, z, z^2, f, zf, f^2\right) dz \tag{23}$$

In addition, the virtual work performed by the elastic subtract is defined by

$$\delta W = -\int_\Omega \left(k_w w - k_s \nabla^2 w\right) \delta w d\Omega \tag{24}$$

in which the symbol ∇ denotes the gradient operator; k_s and k_w, respectively, correspond to the shear and Winkler spring coefficients of the elastic foundation.

By incorporating the corresponding equations into Eq. 20, the motion equation's weak form is reformulated as follows

$$\int_\Omega \delta\bar{\boldsymbol{\varepsilon}}_b^T \bar{\mathbf{D}}_b \bar{\boldsymbol{\varepsilon}}_b d\Omega + \int_\Omega \delta\bar{\boldsymbol{\varepsilon}}_s^T \bar{\mathbf{D}}_s \bar{\boldsymbol{\varepsilon}}_s d\Omega + \int_\Omega \delta\bar{\mathbf{u}}^T \mathbf{I}_m \ddot{\bar{\boldsymbol{u}}} d\Omega + ...$$
$$\int_\Omega \left(k_w w - k_s \nabla^2 w\right) \delta w d\Omega = 0 \tag{25}$$

where

$$\bar{\mathbf{D}}_b = \begin{bmatrix} \mathbf{A}_u & \mathbf{B}_u & \mathbf{C}_u \\ \mathbf{B}_u & \mathbf{D}_u & \mathbf{E}_u \\ \mathbf{C}_u & \mathbf{E}_u & \mathbf{F}_u \end{bmatrix}; \bar{\mathbf{D}}_s = \begin{bmatrix} \mathbf{G}_u & \mathbf{H}_u \\ \mathbf{H}_u & \mathbf{I}_u \end{bmatrix}$$
$$(\mathbf{A}_u, \mathbf{B}_u, \mathbf{C}_u, \mathbf{D}_u, \mathbf{E}_u, \mathbf{F}_u) = \int\limits_{-\frac{h}{2}}^{\frac{h}{2}} \left(1, z, f, z^2, zf, f^2\right) \mathbf{C}_b dz$$
$$(\mathbf{G}_u, \mathbf{H}_u, \mathbf{I}_u) = \int\limits_{-\frac{h}{2}}^{\frac{h}{2}} \left(1, f', f'^2\right) \mathbf{C}_s dz \tag{26}$$

2.3. The MKM approximation

The displacement field $\mathbf{u}^h(\mathbf{x})$ at node $\mathbf{x}$, based on the MKMM [32, 39] is represented approximately as

$$\mathbf{u}^h(\mathbf{x}) = \sum_{j=1}^{N} \mathbf{N}_j(\mathbf{x}) \mathbf{d}_j \tag{27}$$

$$\mathbf{N}_j(\mathbf{x}) = \begin{bmatrix} 1 & 0 & 0 & 0 & 0 & 0 & 0 \\ 0 & 1 & 0 & 0 & 0 & 0 & 0 \\ 0 & 0 & 1 & 0 & 0 & 0 & 0 \\ 0 & 0 & 0 & 1 & 0 & 0 & 0 \\ 0 & 0 & 0 & 0 & 1 & 0 & 0 \\ 0 & 0 & 0 & 0 & 0 & 1 & 0 \\ 0 & 0 & 0 & 0 & 0 & 0 & 1 \end{bmatrix} N_j(\mathbf{x});$$
$$\mathbf{d}_j = \begin{Bmatrix} u_{0j} \\ v_{0j} \\ w_{0j} \\ \beta_{xj} \\ \beta_{yj} \\ \theta_{xj} \\ \theta_{yj} \end{Bmatrix} \tag{28}$$

with $N_j(\mathbf{x})$ represents the MK shape function.

Using the approximation Eq. 27, the bending and shear strain tensors in Eq. 17 and displacement vector $\bar{\mathbf{u}}$ in Eq. 23 are reformed as follows

$$\bar{\boldsymbol{\varepsilon}}_b = \sum_{j=1}^{N} \begin{Bmatrix} \mathbf{B}_{b0j} \\ \mathbf{B}_{b1j} \\ \mathbf{B}_{b2j} \end{Bmatrix} \mathbf{d}_j = \sum_{j=1}^{N} \bar{\mathbf{B}}_{bj} \mathbf{d}_j;$$
$$\bar{\boldsymbol{\varepsilon}}_s = \sum_{j=1}^{N} \begin{Bmatrix} \mathbf{B}_{s0j} \\ \mathbf{B}_{s1j} \end{Bmatrix} \mathbf{d}_j = \sum_{j=1}^{N} \bar{\mathbf{B}}_{sj} \mathbf{d}_j; \tag{29}$$
$$\bar{\mathbf{u}} = \sum_{j=1}^{N} \begin{Bmatrix} \mathbf{B}_{u0j} \\ \mathbf{B}_{u1j} \\ \mathbf{B}_{u2j} \end{Bmatrix} \mathbf{d}_j = \sum_{j=1}^{N} \bar{\mathbf{B}}_{uj} \mathbf{d}_j$$

in which

$$\mathbf{B}_{b0j} = \begin{bmatrix} N_{j,x} & 0 & 0 & 0 & 0 & 0 & 0 \\ 0 & N_{j,y} & 0 & 0 & 0 & 0 & 0 \\ N_{j,y} & N_{j,x} & 0 & 0 & 0 & 0 & 0 \end{bmatrix};$$
$$\mathbf{B}_{b1j} = \begin{bmatrix} 0 & 0 & 0 & -N_{j,x} & 0 & 0 & 0 \\ 0 & 0 & 0 & 0 & -N_{j,y} & 0 & 0 \\ 0 & 0 & 0 & -N_{j,y} & -N_{j,x} & 0 & 0 \end{bmatrix};$$
$$\mathbf{B}_{b2j} = \begin{bmatrix} 0 & 0 & 0 & 0 & 0 & N_{j,x} & 0 \\ 0 & 0 & 0 & 0 & 0 & 0 & N_{j,y} \\ 0 & 0 & 0 & 0 & 0 & N_{j,y} & N_{j,x} \end{bmatrix};$$
$$\mathbf{B}_{s0j} = \begin{bmatrix} 0 & 0 & N_{j,x} & -N_j & 0 & 0 & 0 \\ 0 & 0 & N_{j,y} & 0 & -N_j & 0 & 0 \end{bmatrix};$$
$$\mathbf{B}_{s1j} = \begin{bmatrix} 0 & 0 & 0 & 0 & 0 & N_j & 0 \\ 0 & 0 & 0 & 0 & 0 & 0 & N_j \end{bmatrix}; \tag{30}$$
$$\mathbf{B}_{u0j} = \begin{bmatrix} N_j & 0 & 0 & 0 & 0 & 0 & 0 \\ 0 & N_j & 0 & 0 & 0 & 0 & 0 \\ 0 & 0 & N_j & 0 & 0 & 0 & 0 \end{bmatrix};$$
$$\mathbf{B}_{u1j} = \begin{bmatrix} 0 & 0 & 0 & -N_j & 0 & 0 & 0 \\ 0 & 0 & 0 & 0 & -N_j & 0 & 0 \\ 0 & 0 & 0 & 0 & 0 & 0 & 0 \end{bmatrix};$$
$$\mathbf{B}_{u2j} = \begin{bmatrix} 0 & 0 & 0 & 0 & 0 & N_j & 0 \\ 0 & 0 & 0 & 0 & 0 & 0 & N_j \\ 0 & 0 & 0 & 0 & 0 & 0 & 0 \end{bmatrix}$$

Inserting Eqs. 29 into Eq. 25, for free vibration analysis, the weak form is written in the following form

$$\left(\mathbf{K} - \omega^2\mathbf{M}\right)\bar{\mathbf{d}} = 0 \tag{31}$$

in which

$$\begin{aligned} \mathbf{K} &= \int_\Omega \bar{\mathbf{B}}_b^T\bar{\mathbf{D}}_b\bar{\mathbf{B}}_b \mathrm{d}\Omega + \int_\Omega \bar{\mathbf{B}}_s^T\bar{\mathbf{D}}_s\bar{\mathbf{B}}_s \mathrm{d}\Omega + ... \\ &\int_\Omega \mathbf{B}_e^T\left(k_w\mathbf{B}_e - k_s\nabla^2\mathbf{B}_e\right)\mathrm{d}\Omega \\ \mathbf{M} &= \int_\Omega \bar{\mathbf{B}}_u^T\mathbf{I}_m\bar{\mathbf{B}}_u \mathrm{d}\Omega;\ \mathbf{d} = \bar{\mathbf{d}}\mathrm{e}^{i\omega t} \\ \mathbf{B}_e &= \left\{ \begin{matrix} 0 & 0 & N_j & 0 & 0 & 0 & 0 \end{matrix} \right\} \end{aligned} \tag{32}$$

where ω and $\bar{\mathbf{d}}$ illustrate the natural frequency and mode shapes, respectively; $\mathbf{M}$ denotes the mass matrix, $\mathbf{K}$ denotes the stiffness matrix.

3. Numerical results

In this section, the free vibration of the rectangular, circular and square FGP-GPL plates, as shown in Figure 1, is examined. Based on the theoretical framework of the MKMM, the neutral plane of the FGP-GPL plate is discretized using a set of scattered nodes. In addition, the material parameters used in the analysis are presented as follows:

- For the matrix (Aluminum) [40]: E_m = 70GPa, $\rho_m = 2.702\mathrm{Mg/m^3}$, $\nu_m = 0.3$.
- For the GPLs [33]: E_{GPL} = 1010GPa, ρ_{GPL} = $1.0625\mathrm{Mg/m^3}$, ν_{GPL} = 0.186, $l_{GPL} = 2.5 \cdot 10^{-6}$ m, $w_{GPL} = 1.5 \cdot 10^{-6}$ m, $t_{GPL} = 1.5 \cdot 10^{-9}$ m.

Furthermore, the FGP-GPL plates are studied under various boundary conditions (BCs), including SSSS, CCCC, SCSC for rectangular plates and SS, CC for circular plates. The boundary condition types are presented in Table 2, where, the 'S' and 'C' respectively indicate the simply supported and clamped boundaries. Finally, the dimensionless quantities used for examining the FGP-GPL plate's vibration are determined as follows

$$\begin{aligned} \Omega &= \omega a\sqrt{\frac{\rho_m}{E_m}}, K_w = \frac{k_w a^4}{D_m}, \\ K_s &= \frac{k_s a^2}{D_m}, D_m = \frac{E_m h^3}{12(1-{\nu_m}^2)} \end{aligned} \tag{33}$$

Tab. 2: Types of boundary conditions.

Types	Condition
SSSS	$\left\{ \begin{array}{l} (u_0, w_0, \beta_x, \theta_x) = 0;\ \text{at } y = 0, b \\ (v_0, w_0, \beta_y, \theta_y) = 0;\ \text{at } x = 0, a \end{array} \right.$
CCCC	$\left\{ \begin{array}{l} (u_0, v_0, w_0, \beta_x, \beta_y, \theta_x, \theta_y) = 0;\ \text{at } y = 0, b \\ (u_0, v_0, w_0, \beta_x, \beta_y, \theta_x, \theta_y) = 0;\ \text{at } x = 0, a \end{array} \right.$
SCSC	$\left\{ \begin{array}{l} (u_0, v_0, w_0, \beta_x, \beta_y, \theta_x, \theta_y) = 0;\ \text{at } y = 0, b \\ (v_0, w_0, \beta_y, \theta_y) = 0;\ \text{at } x = 0, a \end{array} \right.$
SS	$(u_0, v_0, w_0) = 0;$ at the boundary
CC	$(u_0, v_0, w_0, \beta_x, \beta_y, \theta_x, \theta_y) = 0;$ at the boundary

3.1. Verification

To verify the reliability of the computational model for the vibration analysis of the FGP-GPL square plate is examined. Table 3 lists the initial non-dimensional modal frequencies $\varpi = \omega a\sqrt{\rho_m\left(1-{\nu_m}^2\right)/E_m}$ of these plates, with material parameters taken from Ref. [33]. These results are validated with the reference solutions provided by Yang *et al.* [33], which were obtained through the application of FSDT along with an analytical approach. As shown in Table 3, the results match very closely with the reference solutions. To further enhance the reliability of this research, we conduct an additional study on the vibration of the multilayer functionally graded composite plates reinforced with graphene platelets (MFG-GPLRC). The GPLs weight fraction varies from layer to layer along the thickness direction, following four different distribution pattern UD, FG-O, FG-X and FG-A, as illustrated in Figure 4. Moreover, the material properties of the MFG-GPLRC are taken as follows: $E_m = 3\text{GPa}$, $\nu_m = 0.34$, $\rho_m = 1200\text{kg/m}^3$ for the polymer matrix [42] and $E_{GPL} = 1.01\text{TPa}$, $\nu_{GPL} = 0.186$, $\rho_{GPL} = 1060\text{kg/m}^3$, $l_{GPL} = 2.5\mu m$, $w_{GPL} = 1.5\mu m$, $h_{GPL} = 1.5nm$ for the GPLs [41]. Table 4 presents the lowest eight non-dimensional frequencies $\bar{\Omega} = \omega h\sqrt{\rho_m/E_m}$ of MFG-GPLRC plates. The obtained results are compared with those reported by Song *et al.* [42] and Arefi *et al.* [43] using the Navier method in combination with FSDT, by Reddy et al. [44] using FEM and FSDT, by Thai *et al.* [45] employing IGA based on HSDT. Once again, the results in Table 4 are in close agreement with those references. The comparison results presented in Table 3 and Table 4 indicate that the proposed model yields accurate predictions.

3.2. Rectangular plates

Let's examine the behavior of the FGP-GPL rectangular plate resting on an elastic foundation. Firstly, we investigate how porosity and GPL distributions affect the initial six normalized modal frequencies (Ω) of FGP-GPL square plates is presented in Table 5. For all cases, the P-I porosity configuration yields the greatest frequency, whereas plates with the P-II porosity distribution provide the lowest. This is because, during bending, the top and bottom surfaces of the FGP-GPL plate undergo the highest tensile and compressive stresses, while the middle region has significantly lower deformation and stress. In the P-I distribution, pores are mainly concentrated in the core region, resulting in higher Young's modulus near the outer surfaces. This enhances the bending stiffness and provides better resistance to deformation compared to the P-II distribution. Moreover, maximum and minimum vibrational frequencies are found in the GPL-A and GPL-B distributions. In addition, the CCCC FGP-GPL plate exhibits the peak normalized vibration frequency, while the SSSS plate yields the lowest. Next, Figure 5 illustrates how the porosity coefficient e_0 affects on the lowest normalized modal frequency of the square plate with FGP-GPL reinforcement. Based on the data from Figure 5, raising the porosity coefficient causes the frequency of the plate to drop. This is because a higher porosity coefficient reduces the Young's modulus of the FGP-GPL plate, leading to lower stiffness and natural frequency. Moving forward, Figure 6 illustrates the relationship between GPL weight fraction (W_{GPL}) and the first non-dimensional frequency considering different distribution patterns. This chart demonstrates the significant impact of GPLs on the overall stiffness of the plate. As the weight fraction increases, the stiffness also increases significantly. When the GPLs dispersed into the matrix, they significantly enhance the mechanical properties of the FGP plate, such as the Young's modulus, while contributing negligibly to the overall mass. In addition, the GPL-A plate exhibits the greatest increase in the dimensionless vibration frequency, whereas the GPL-B plate shows the smallest. The influence of the length-to-thickness ratio a/h on the lowest dimensionless frequency of the FGP-GPL plate is plotted in Figure 7. Increasing the coefficient a/h leads to a lowering of the FGP-GPL plate's frequency. Besides, Figure 8 shows the effect of the width-to-length ratio b/a on the lowest normalized frequency of the FGP-GPL plate. From Figure 8, the natural frequency of the FGP-GPL plate decreases while the b/a ratio increases. The effects of the dimensionless spring and shear parameters on the plate's frequency are displayed in Table 6. As the spring and shear parameters increase, the plate's frequency also increases significantly. Finally, the lowest six vibration modes of the FGP-GPL plate under CCCC boundaries are shown in Figure 9.

3.3. Circular plates

This section presents an analysis of the free vibrational response of the FGP-GPL circular plate. Two types of boundary conditions are examined, as presented in Table 2. Furthermore, the non-dimensional parameters are defined as follows:

$$\Omega_c = \omega R\sqrt{\frac{\rho_m}{E_m}}, K_{wc} = \frac{k_w R^4}{D_m}, K_{sc} = \frac{k_s R^2}{D_m} \quad (34)$$

Firstly, the effect of porosity and GPL distributions on the initial six dimensionless frequencies (Ω_c) of the circular plate embedded with FGP-GPL is presented in Table 7. Among the considered cases, the P-I porosity shows the largest modal frequency. In addition, the P-III plate has a medium frequency, while the P-II plate has the lowest. For each porosity distribution, the GPL-A reinforcement offers the most effective improvement in vibrational stiffness. Therefore, the GPL-A has the highest vibration frequency, while the GPL-B plate has the lowest. Moreover, the GPL-C plate has a uniform GPLs distribution, so the vibration frequency can be improved moderately. Finally, the CC FGP-GPL plate has a higher frequency than the SS FGP-GPL plate. Next, Figure 10 illustrates the impact of the porous coefficient e_0 on the lowest non-dimensional frequency with different porosity distributions. When the porosity coefficient increases, the frequency of the P-I plate decreases slightly. However, the frequencies of other porosity distributions decrease much more rapidly. Furthermore, the P-III plate has a uniform porosity distribution, so its stiffness reduces moderately. The P-II plate, on the other hand, shows the most significant reduction in the vibrational frequency. Moving forward, Figure 11 illustrates the effect of the GPLs weight fraction W_{GPL} on the lowest dimensionless natural frequency with different GPLs distributions. Increasing the GPLs weight fraction improves the stiffness of the plate. According to Figure 11, the GPL-A plate exhibits the most significant increases in frequency, while the GPL-B has the most minor increases. The effect of the radius-to-thickness ratio R/h on the lowest dimensionless natural frequency is presented in Figure 12. When the R/h ratio rises, the plate's stiffness reduces, resulting in a lower vibrational frequency. In addition, Table 8 demonstrates the effects of the normalized spring and shear coefficients on the lowest dimensionless frequency of the FGP-GPL plate, respectively. Increasing the Winkler-Pasternak foundation's spring and shear coefficients enhances the plate's stiffness, resulting in a higher natural frequency. Finally, Figure 13 illustrates the first six mode shapes of the FGP-GPL circular plate under CC boundary conditions.

3.4. Square plates with a cutout heart

Next, we investigate one more geometry of the FGP-GPL plate. A square plate with a cutout heart as shown in Figure 1 is considered. This type of structure is very common in practical applications, as the plate or shell structures are rarely perfectly intact. They are often designed with holes to enable connections with other components. Firstly, Table 9 illustrates the impact of porosity and GPLs distributions on the lowest six dimensionless frequencies (Ω) of FGP-GPL square plates. Once again, the highest stiffness belongs to P-I porosity and GPL-A pattern as shown in Table 9. In contrast, the P-II and GPL-B distribution yield the lowest vibrational frequency.

Additionally, the plate with fully clamped boundary conditions exhibits the highest frequency. Next, Table 10 describes the influence of the dimensionless spring and shear parameters on the non-dimensional natural frequency of the FGP-GPL plate. The data in Table 10 indicate that the vibrational stiffness of the plate improves when these coefficients increase.

Tab. 3: The lowest dimensionless frequency of the FGP-GPL plate involving various porous and GPL dispersions ($a = b$, $e_0 = 0.5$, $W_{GPL} = 0.01$, $K_w = K_s = 0$).

Porous	Type GPLs	a/h							
		20		30		40		50	
		Present	Ref. [33]	Present	Ref. [33]	Present	Ref. [33]	Present	Ref. [33]
CCCC									
P-I	GPL-	0.6961	0.7022	0.4778	0.4783	0.3624	0.3616	0.2915	0.2904
	GPL-B	0.5881	0.5883	0.3989	0.3987	0.3012	0.3008	0.2417	0.2413
	GPL-C	0.6361	0.6366	0.4331	0.4324	0.3275	0.3265	0.2631	0.262
P-II	GPL-A	0.5477	0.5502	0.3706	0.372	0.2795	0.2805	0.2242	0.2249
	GPL-B	0.4676	0.4686	0.3148	0.3155	0.237	0.2375	0.1899	0.1903
	GPL-C	0.4941	0.4953	0.333	0.3339	0.2508	0.2515	0.2011	0.2016
P-III	GPL-A	0.6435	0.6456	0.4389	0.4387	0.332	0.3313	0.2668	0.2659
	GPL-B	0.5405	0.5402	0.3653	0.3652	0.2755	0.2753	0.221	0.2207
	GPL-C	0.5821	0.5814	0.3945	0.3938	0.2977	0.2971	0.2389	0.2383
SSSS									
P-I	GPL-A	0.3969	0.3958	0.2671	0.2657	0.201	0.1997	0.161	0.16
	GPL-B	0.3299	0.3293	0.2212	0.2207	0.1662	0.1658	0.1331	0.1328
	GPL-C	0.3588	0.3574	0.2408	0.2397	0.181	0.1801	0.145	0.1442
P-II	GPL-A	0.3063	0.3072	0.2051	0.2057	0.1541	0.1545	0.1234	0.1237
	GPL-B	0.2596	0.2601	0.1736	0.174	0.1303	0.1306	0.1043	0.1046
	GPL-C	0.2748	0.2754	0.1838	0.1843	0.138	0.1384	0.1105	0.1108
P-III	GPL-A	0.3638	0.3627	0.2442	0.2433	0.1837	0.1828	0.1471	0.1464
	GPL-B	0.3017	0.3014	0.2021	0.2018	0.1518	0.1516	0.1215	0.1214
	GPL-C	0.3262	0.3252	0.2186	0.2179	0.1643	0.1637	0.1315	0.1311

Tab. 4: The lowest eight dimensionless frequencies of the SSSS MFG-GPLRC square plate with various GPLs distributions ($a/h = 10$, $N_L = 10$, $W_{GPL} = 0.01$, $K_w = K_s = 0$).

Types	Mode	Present	Navier-FSDT [42]	Navier-FSDT [43]	Navier-SSDT [43]	FEM-FSDT [44]	IGA-HSDT [45]
Pure epoxy	1	0.0584	0.0584	0.0584	0.0584	0.0588	0.0584
	2	0.139	0.1391	0.1391	0.1391	0.1412	0.1391
	3	0.1391	0.1391	0.1391	0.1391	0.1412	0.1391
	4	0.213	0.2132	0.2132	0.2133	0.2176	0.2132
	5	0.2591	0.2595	0.2595	0.2597	0.2176	0.2596
	6	0.2595	0.2595	0.2595	0.2597	0.2658	0.2596
	7	0.3248	0.3251	0.3251	0.3254	0.3341	0.3254
	8	0.3251	0.3251	0.3251	0.3254	0.3341	0.3254
UD	1	0.1215	0.1216	0.1216	0.1216	0.1225	0.1216
	2	0.2892	0.2895	0.2895	0.2896	0.2941	0.2895
	3	0.2894	0.2895	0.2895	0.2896	0.2941	0.2895
	4	0.4433	0.4436	0.4436	0.4438	0.4531	0.4437
	5	0.5393	0.54	0.54	0.5403	0.4531	0.5403
	6	0.5401	0.54	0.54	0.5403	0.5535	0.5403
	7	0.676	0.6767	0.6767	0.6773	0.6956	0.6771
	8	0.6765	0.6767	0.6767	0.6773	0.6956	0.6771
FG-O	1	0.1022	0.102	0.102	0.1023	0.0912	0.1023
	2	0.2467	0.2456	0.2456	0.2471	0.2246	0.247
	3	0.2468	0.2456	0.2456	0.2471	0.2246	0.247
	4	0.3822	0.3796	0.3796	0.383	0.3532	0.3828
	5	0.4681	0.4645	0.4645	0.4694	0.3532	0.4692
	6	0.4687	0.4645	0.4645	0.4694	0.4378	0.4692
	7	0.5917	0.586	0.586	0.5934	0.5581	0.5931
	8	0.5922	0.586	0.586	0.5934	0.5581	0.5931
FG-X	1	0.1364	0.1378	0.1378	0.1365	0.142	0.1366
	2	0.318	0.3249	0.3249	0.3183	0.3245	0.3189
	3	0.3182	0.3249	0.3249	0.3183	0.3245	0.3189
	4	0.4794	0.4939	0.4939	0.4798	0.481	0.4809
	5	0.5779	0.5984	0.5984	0.5787	0.481	0.5805
	6	0.5787	0.5984	0.5984	0.5787	0.575	0.5805
	7	0.7159	0.7454	0.7454	0.7168	0.7031	0.7192
	8	0.7165	0.7454	0.7454	0.7168	0.7031	0.7192
FG-A	1	0.1117	0.1118	0.1118	0.1118	0.108	0.1118
	2	0.2671	0.2673	0.2673	0.2671	0.2589	0.2674
	3	0.2673	0.2673	0.2673	0.2671	0.2589	0.2674
	4	0.4107	0.411	0.411	0.4107	0.4088	0.4111
	5	0.5007	0.5013	0.5013	0.5009	0.4088	0.5016
	6	0.5014	0.5013	0.5013	0.5009	0.5009	0.5016
	7	0.6292	0.6299	0.6299	0.6294	0.6351	0.6303
	8	0.6297	0.6299	0.6299	0.6294	0.6351	0.6303

Tab. 5: The lowest eight dimensionless frequencies of the SSSS MFG-GPLRC square plate with various GPLs distributions ($a/h = 10$, $e_0 = 0.1$, $W_{GPL} = 0.01$, $K_w = K_s = 0$).

Type		Mode					
Porosity distribution	GPL pattern	1	2	3	4	5	6
		SSSS					
P-I	GPL-A	0.7216	1.7002	1.7014	2.5845	3.1302	3.1347
	GPL-B	0.6336	1.5165	1.5175	2.3345	2.8477	2.8517
	GPL-C	0.6685	1.5919	1.593	2.4405	2.9699	2.9742
P-II	GPL-A	0.6971	1.6508	1.6519	2.5195	3.0582	3.0626
	GPL-B	0.6118	1.4693	1.4702	2.2682	2.7713	2.7753
	GPL-C	0.6442	1.5406	1.5416	2.3697	2.8893	2.8935
P-III	GPL-A	0.7128	1.6825	1.6837	2.5614	3.1048	3.1093
	GPL-B	0.6256	1.4993	1.5003	2.3104	2.8201	2.8241
	GPL-C	0.6597	1.5733	1.5744	2.415	2.941	2.9453
		CCCC					
P-I	GPL-A	1.2064	2.266	2.2738	3.1581	3.6976	3.7383
	GPL-B	1.0869	2.0814	2.0889	2.9329	3.4624	3.4986
	GPL-C	1.137	2.1632	2.1709	3.0364	3.5744	3.6125
P-II	GPL-A	1.1742	2.2186	2.2263	3.1022	3.6409	3.6803
	GPL-B	1.0549	2.0291	2.0365	2.8671	3.3913	3.4261
	GPL-C	1.1027	2.1088	2.1163	2.9692	3.5031	3.5398
P-III	GPL-A	1.1949	2.2494	2.2571	3.1387	3.6781	3.7183
	GPL-B	1.0753	2.0626	2.07	2.9093	3.437	3.4727
	GPL-C	1.1246	2.1437	2.1514	3.0126	3.5492	3.5869
		SCSC					
P-I	GPL-A	0.9929	1.8247	2.166	2.8807	3.1936	3.6559
	GPL-B	0.8885	1.6417	1.9841	2.6474	2.9155	3.4172
	GPL-C	0.9316	1.7182	2.064	2.7509	3.0369	3.53
P-II	GPL-A	0.9645	1.776	2.1191	2.8215	3.123	3.5981
	GPL-B	0.8612	1.5936	1.9331	2.5821	2.8396	3.3456
	GPL-C	0.902	1.6664	2.0107	2.6829	2.9571	3.4579
P-III	GPL-A	0.9827	1.8073	2.1495	2.8599	3.1687	3.6359
	GPL-B	0.8786	1.6242	1.9657	2.6239	2.8881	3.3916
	GPL-C	0.9209	1.6995	2.0449	2.7266	3.0083	3.5046

Tab. 6: The impact of the spring and shear parameters on the initial non-dimensional frequency the square plate containing FGP-GPL (P-III, GPL-A, $a = 20h,\ e_0 = 0.2,\ W_{GPL} = 0.02$).

BCs	K_w	K_s					
		0	2	4	6	8	10
SSSS	0	0.4232	0.4348	0.4461	0.4571	0.4678	0.4784
	20	0.4291	0.4405	0.4517	0.4626	0.4732	0.4836
	40	0.4349	0.4462	0.4572	0.468	0.4785	0.4888
	60	0.4406	0.4518	0.4627	0.4733	0.4837	0.4939
	80	0.4463	0.4573	0.4681	0.4786	0.4889	0.4990
	100	0.4519	0.4628	0.4734	0.4838	0.494	0.5040
CCCC	0	0.7483	0.7562	0.764	0.7717	0.7793	0.7868
	20	0.7517	0.7595	0.7673	0.7749	0.7825	0.7900
	40	0.755	0.7628	0.7705	0.7782	0.7857	0.7932
	60	0.7583	0.7661	0.7738	0.7814	0.7889	0.7964
	80	0.7617	0.7694	0.777	0.7846	0.7921	0.7995
	100	0.765	0.7727	0.7803	0.7878	0.7953	0.8027
SCSC	0	0.6066	0.6155	0.6243	0.633	0.6415	0.6499
	20	0.6108	0.6196	0.6284	0.637	0.6454	0.6538
	40	0.6149	0.6237	0.6323	0.6409	0.6493	0.6577
	60	0.6189	0.6277	0.6363	0.6448	0.6532	0.6615
	80	0.623	0.6317	0.6403	0.6487	0.657	0.6653
	100	0.627	0.6357	0.6442	0.6526	0.6609	0.669

Tab. 7: Fundamental dimensionless frequencies (first six modes) for the FGP-GPL circular plate ($R = 10h,\ e_0 = 0.1,\ W_{GPL} = 0.01,\ K_{wc} = K_{sc} = 0$).

Type		Mode					
Porosity distribution	GPL pattern	1	2	3	4	5	6
		SS					
P-I	GPL-A	0.1865	0.5129	0.5152	0.9185	0.9268	1.0652
	GPL-B	0.1623	0.4491	0.4516	0.8107	0.8196	0.9405
	GPL-C	0.1717	0.4743	0.4767	0.8538	0.8626	0.9905
P-II	GPL-A	0.1796	0.495	0.4973	0.8886	0.8971	1.0308
	GPL-B	0.1564	0.4334	0.436	0.7837	0.7927	0.9092
	GPL-C	0.1651	0.4567	0.4592	0.824	0.8329	0.9559
P-III	GPL-A	0.184	0.5064	0.5087	0.9077	0.9161	1.0528
	GPL-B	0.1601	0.4434	0.4459	0.8008	0.8098	0.929
	GPL-C	0.1693	0.4678	0.4703	0.843	0.8517	0.9779
		CC					
P-I	GPL-A	0.3755	0.7564	0.7587	1.2013	1.2049	1.3576
	GPL-B	0.3294	0.6697	0.6717	1.0735	1.0768	1.216
	GPL-C	0.3476	0.7046	0.7068	1.126	1.1295	1.2745
P-II	GPL-A	0.3626	0.7324	0.7347	1.1666	1.1702	1.3194
	GPL-B	0.318	0.6477	0.6496	1.0403	1.0435	1.1789
	GPL-C	0.3349	0.6805	0.6825	1.09	1.0933	1.2345
P-III	GPL-A	0.3708	0.7477	0.75	1.1889	1.1925	1.3439
	GPL-B	0.3252	0.6617	0.6637	1.0614	1.0646	1.2025
	GPL-C	0.343	0.6959	0.6979	1.113	1.1164	1.26

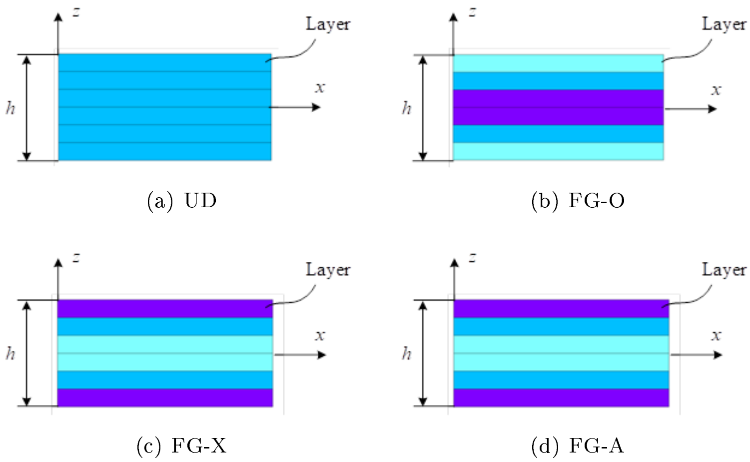

Fig. 4: GPLs distributions of the MFG-GPLRC plates.

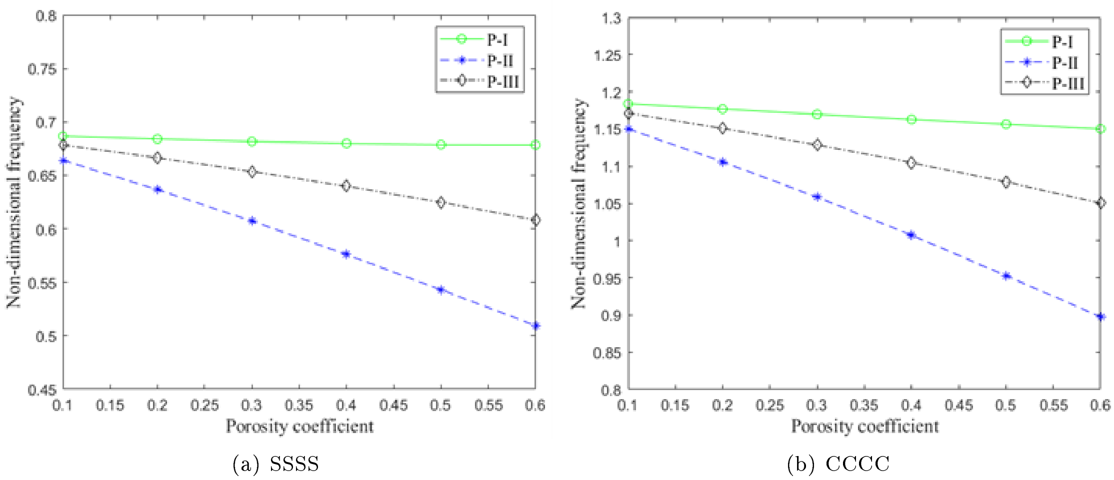

Fig. 5: The relationship between parameter e0 and the FGP-GPL square plate's first non-dimensional natural frequency (GPL-B, $a/h = 10$, $W_{GPL} = 0.02$, $K_w = K_s = 0$).

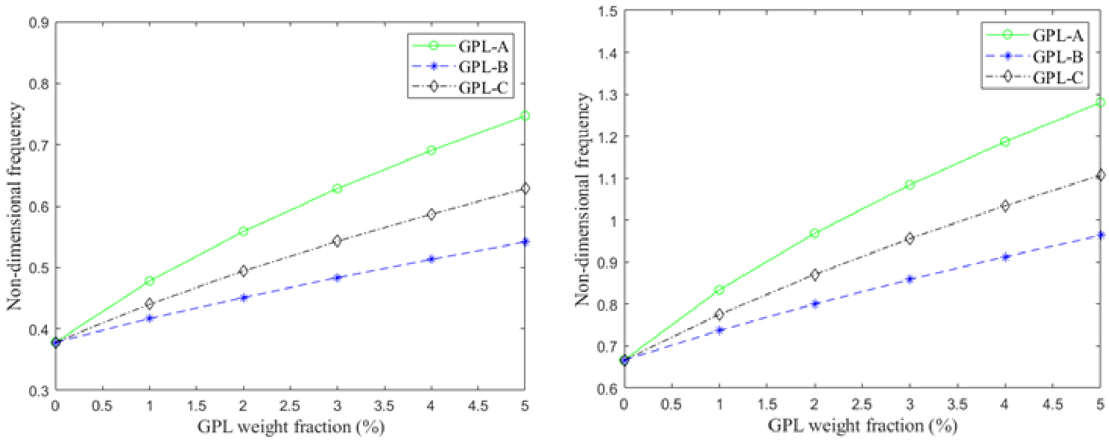

(a) SSSS (b) CCCC

Fig. 6: Variation of the FGP-GPL square plate's first non-dimensional frequency with respect to the GPL weight fraction (P-III, $a = 15h$, $e_0 = 0.2$, $K_w = K_s = 0$).

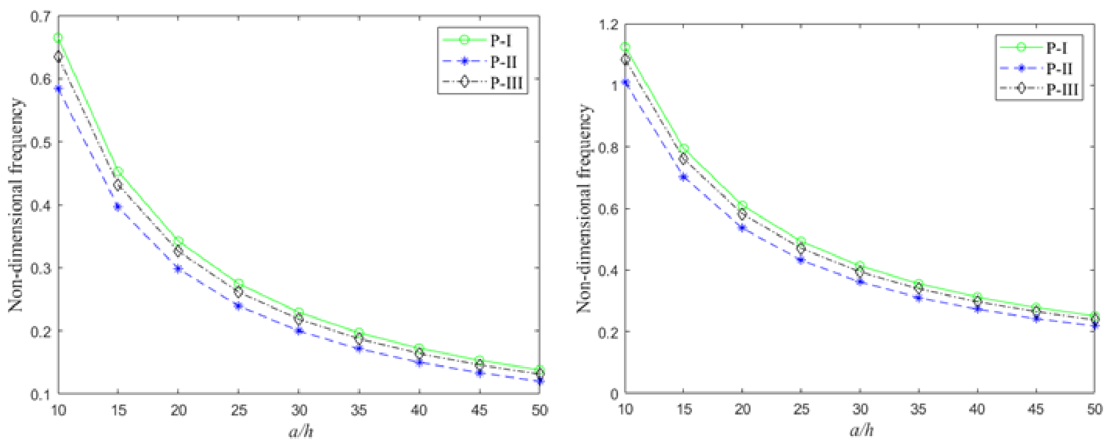

(a) SSSS (b) CCCC

Fig. 7: Effect of the a/h ratio on the initial non-dimensional frequency of the FGP-GPL square plate (GPL-C, $e_0 = 0.3$, $W_{GPL} = 0.01$, $K_w = K_s = 0$).

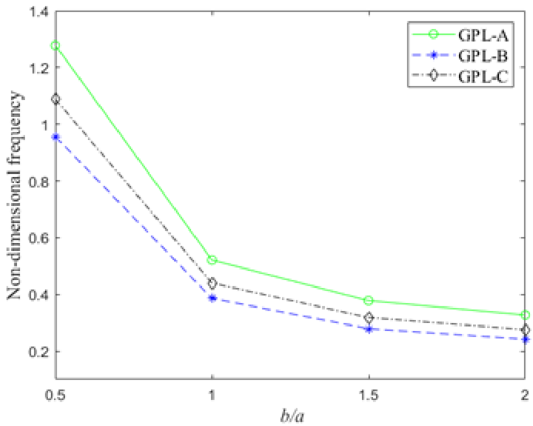

(a) SSSS

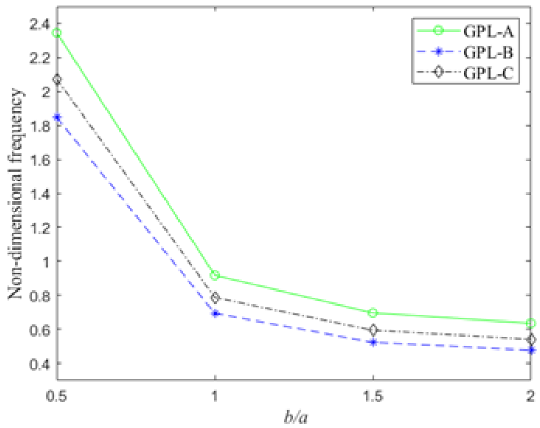

(b) CCCC

Fig. 8: The impact of the width-to-length ratio on the lowest normalized frequency of the FGP-GPL rectangular plate (P-II, $a = 20h$, $e_0 = 0.1$, $W_{GPL} = 0.04$, $K_w = K_s = 0$).

Tab. 8: The impact of the spring and shear parameters on the initial non-dimensional frequency the circular plate containing FGP-GPL (P-III, GPL-A, $R = 20h$, $e_0 = 0.2$, $W_{GPL} = 0.02$) .

BCs	K_{wc}	K_{sc}					
		0	2	4	6	8	10
SS	0	0.1066	0.1195	0.1312	0.1419	0.1518	0.1612
	20	0.1281	0.1391	0.1492	0.1587	0.1677	0.1761
	40	0.1465	0.1562	0.1653	0.1739	0.1821	0.1899
	60	0.1628	0.1716	0.1799	0.1878	0.1955	0.2028
	80	0.1777	0.1857	0.1934	0.2008	0.208	0.2149
	100	0.1914	0.1988	0.2061	0.213	0.2198	0.2263
CC	0	0.2194	0.2271	0.2345	0.2417	0.2487	0.2554
	20	0.2306	0.238	0.2451	0.252	0.2586	0.2651
	40	0.2413	0.2483	0.2552	0.2618	0.2682	0.2745
	60	0.2516	0.2583	0.2649	0.2713	0.2775	0.2835
	80	0.2614	0.2679	0.2742	0.2804	0.2864	0.2923
	100	0.2709	0.2772	0.2833	0.2893	0.2951	0.3008

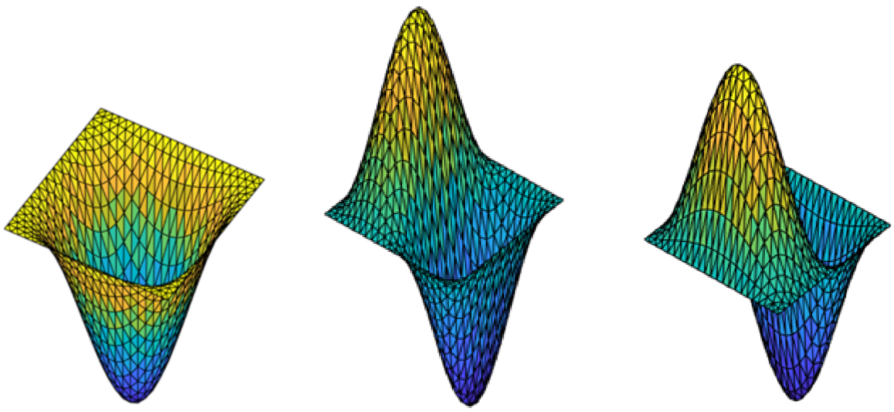

(a) Mode 1 ($\Omega = 1.3169$) (b) Mode 2 ($\Omega = 2.3403$) (c) Mode 3 ($\Omega = 2.3474$)

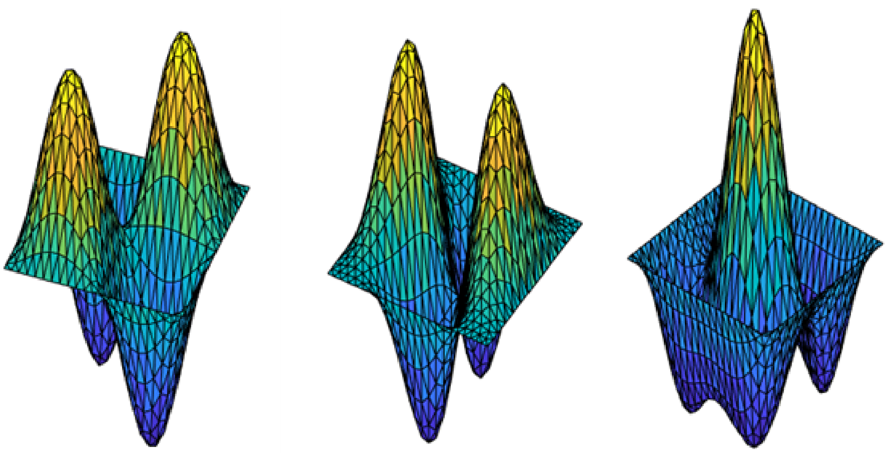

(d) Mode 4 ($\Omega = 3.1992$) (e) Mode 5 ($\Omega = 3.7115$) (f) Mode 6 ($\Omega = 3.7485$)

Fig. 9: The first six mode shapes of the FGP-GPL square plate under CCCC boundaries (P-I, GPL-A, $a = 10h$, $e_0 = 0.4$, $W_{GPL} = 0.01$, $K_w = 100$, $K_s = 10$).

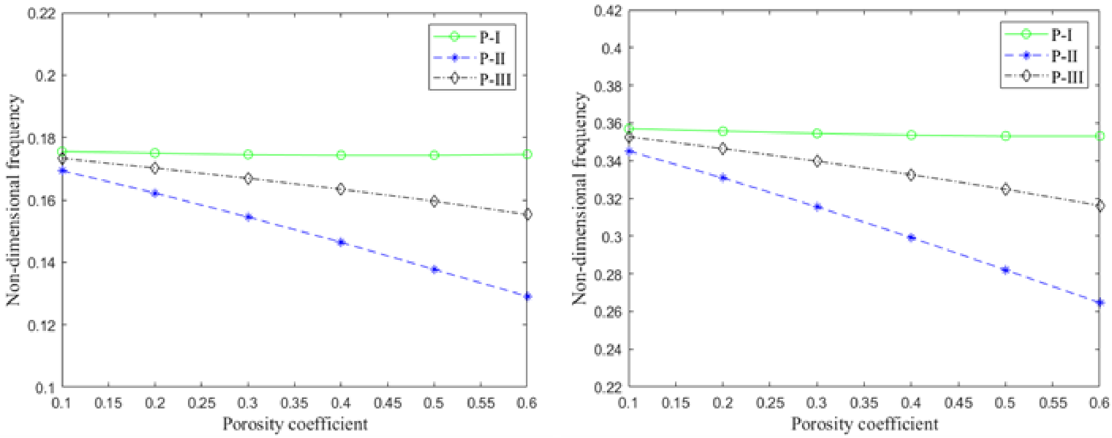

(a) SS (b) CC

Fig. 10: Dependency of the first non-dimensional natural frequency of the FGP-GPL circular plate on the parameter e_0 (GPL-B, $R = 10h$, $W_{GPL} = 0.02$, $K_{wc} = K_{sc} = 0$).

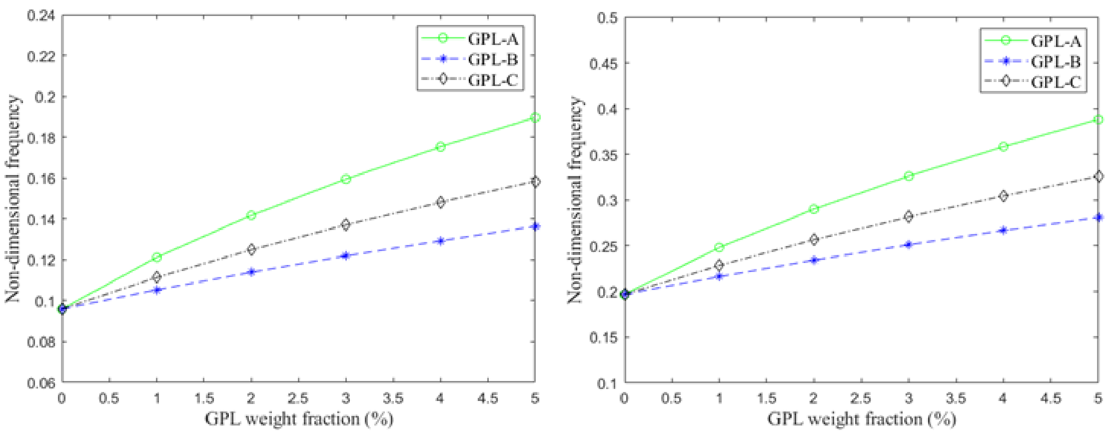

(a) SS (b) CC

Fig. 11: The effect of the GPL weight fraction on the lowest non-dimensional natural frequency of the FGP-GPL circular plate (P-III, $R = 15h$, $e_0 = 0.02$, $K_{wc} = K_{sc} = 0$).

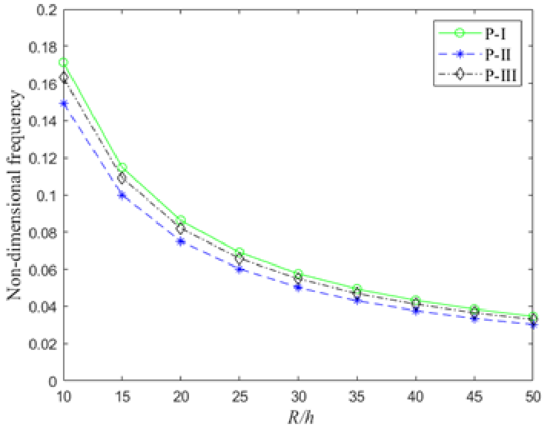

(a) SS (b) CC

Fig. 12: The impact of the R/h ratio on the lowest natural frequency in dimensionless form of the circular plate containing FGP-GPL (GPL-C, $e_0 = 0.03$, $W_{GPL} = 0.01$, $K_{wc} = K_{sc} = 0$).

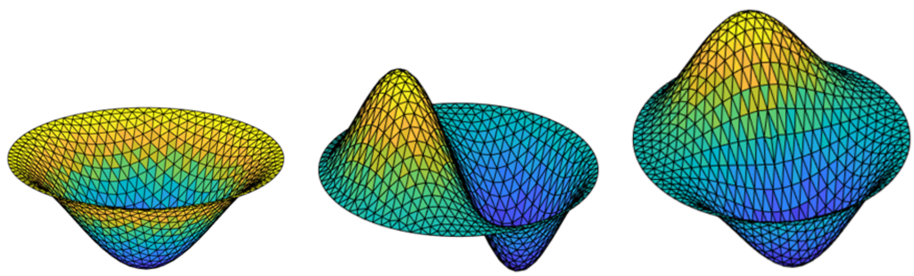

(a) Mode 1 ($\Omega_c = 0.5629$) (b) Mode 2 ($\Omega_c = 0.9123$) (c) Mode 3 ($\Omega_c = 0.9144$)

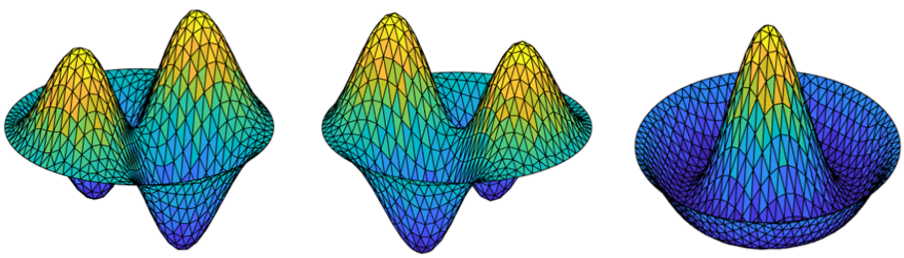

(d) Mode 4 ($\Omega_c = 1.3369$) (e) Mode 5 ($\Omega_c = 1.3403$) (f) Mode 6 ($\Omega_c = 1.4853$)

Fig. 13: The first six mode shapes of the FGP-GPL circular plate (CC, P-I, GPL-A, $R = 10h$, $e_0 = 0.4$, $W_{GPL} = 0.01$, $K_{wc} = 100$, $K_{sc} = 10$).

Tab. 9: Fundamental dimensionless frequencies (first six modes) for the FGP-GPL square plate with a cutout heart ($a = 10h,\ e_0 = 0.1,\ W_{GPL} = 0.01,\ K_w = K_s = 0$).

Type		Mode					
Porosity distribution	GPL pattern	1	2	3	4	5	6
		SSSS					
P-I	GPL-A	0.8632	1.3308	1.5044	2.3438	2.4523	3.397
	GPL-B	0.7566	1.1885	1.343	2.1157	2.2308	3.1175
	GPL-C	0.7986	1.2464	1.4088	2.2116	2.3254	3.2408
P-II	GPL-A	0.8342	1.2934	1.4621	2.2852	2.3965	3.3281
	GPL-B	0.731	1.1535	1.3031	2.057	2.1733	3.0418
	GPL-C	0.7701	1.2081	1.3652	2.1486	2.2642	3.1617
P-III	GPL-A	0.8527	1.3174	1.4892	2.3229	2.4325	3.3728
	GPL-B	0.7472	1.1758	1.3284	2.0944	2.21	3.0902
	GPL-C	0.7882	1.2325	1.393	2.1889	2.3034	3.2126
		CCCC					
P-I	GPL-A	1.7315	2.8421	2.8697	3.3738	3.4527	4.0655
	GPL-B	1.5721	2.6164	2.6396	3.1316	3.2113	3.8107
	GPL-C	1.6399	2.7166	2.7414	3.2418	3.3219	3.9311
P-II	GPL-A	1.6899	2.7859	2.8122	3.3147	3.3944	4.0053
	GPL-B	1.5298	2.5543	2.5766	3.0639	3.1435	3.737
	GPL-C	1.5947	2.6519	2.6756	3.1719	3.2523	3.8565
P-III	GPL-A	1.7167	2.8223	2.8495	3.3532	3.4324	4.0447
	GPL-B	1.5568	2.594	2.6169	3.1073	3.1869	3.7843
	GPL-C	1.6237	2.6935	2.7179	3.2169	3.2972	3.9048
		SCSC					
P-I	GPL-A	1.3133	1.6319	2.3996	2.8416	3.1748	3.7514
	GPL-B	1.18	1.4763	2.1915	2.6105	2.9312	3.4771
	GPL-C	1.2352	1.5416	2.2817	2.7123	3.0403	3.6017
P-II	GPL-A	1.2781	1.5921	2.3469	2.7841	3.115	3.6852
	GPL-B	1.1457	1.4367	2.1357	2.5479	2.8642	3.4009
	GPL-C	1.1982	1.4991	2.2228	2.6468	2.9707	3.5232
P-III	GPL-A	1.3007	1.6177	2.381	2.8214	3.1538	3.7283
	GPL-B	1.1675	1.462	2.1713	2.588	2.9071	3.4497
	GPL-C	1.2219	1.5263	2.2606	2.6889	3.0155	3.5738

Tab. 10: The impact of the spring and shear parameters on the initial non-dimensional frequency the FGP-GPL square plate with a cutout heart (P-III, GPL-A, $a = 20h$, $e_0 = 0.2$, $W_{GPL} = 0.02$).

BCs	K_w	K_s					
		0	2	4	6	8	10
SSSS	0	0.5136	0.5197	0.5257	0.5316	0.5374	0.5432
	20	0.5185	0.5245	0.5304	0.5363	0.5421	0.5478
	40	0.5233	0.5292	0.5351	0.5409	0.5467	0.5523
	60	0.5281	0.534	0.5398	0.5455	0.5512	0.5569
	80	0.5328	0.5386	0.5444	0.5501	0.5558	0.5613
	100	0.5375	0.5432	0.549	0.5546	0.5602	0.5658
CCCC	0	1.1107	1.1133	1.1158	1.1184	1.121	1.1236
	20	1.1129	1.1155	1.1181	1.1206	1.1232	1.1258
	40	1.1152	1.1177	1.1203	1.1229	1.1254	1.128
	60	1.1174	1.12	1.1225	1.1251	1.1277	1.1302
	80	1.1196	1.1222	1.1248	1.1273	1.1299	1.1324
	100	1.1219	1.1244	1.127	1.1295	1.1321	1.1346
SCSC	0	0.8227	0.827	0.8313	0.8355	0.8398	0.8439
	20	0.8257	0.83	0.8343	0.8385	0.8427	0.8469
	40	0.8288	0.8331	0.8373	0.8415	0.8457	0.8499
	60	0.8318	0.8361	0.8403	0.8445	0.8487	0.8528
	80	0.8348	0.839	0.8433	0.8474	0.8516	0.8557
	100	0.8378	0.842	0.8462	0.8504	0.8545	0.8586

4. Conclusions

This study investigates the behavior of the FGP-GPL plate resting on an elastic foundation using the C0-HSDT and MKMM. The FGP-GPL plate is analyzed using different types of porosity and GPL distributions. In addition, they are both distributed through the plate's thickness. The MKMM is used to obtain the mode shapes and natural frequencies of the FGP-GPL plates. The results show that the FGP-GPL plate with P-I and GPL-A distributions exhibits the peak of natural frequency, while the plate with P-II and GPL-B exhibits the lowest. Furthermore, increasing the porosity coefficient leads to a reduction in the stiffness and vibrational frequency of the FGP-GPL plate. Next, a rise in the GPL weight fraction improves the frequency of the plate. In contrast, when the length-to-radius, length-to-thickness and width-to-length ratios increase, the FGP-GPL plate stiffness becomes smaller. In addition, this study also demonstrates that an increase in the non-dimensional spring and shear parameters of the Winkler-Pasternak foundation leads to a significant enhancement of the natural frequency of the plate. Finally, the findings of this paper can be utilized to optimize and develop these structures for real-life applications across different fields. This study can be further extended to analyze the stability or forced vibration behavior of the FGP-GPL plate.

Acknowledgment

This work belongs to the project grant No: SV2025-312 funded by Ho Chi Minh city University of Technology and Education, Vietnam.

References

[1] M. F. Ashby. Metal foams: a design guide. *Elsevier*, 2000.

[2] N. Dukhan. Metal foams: fundamentals and applications. *DEStech Publ.*, 2013.

[3] A. K. Geim. Graphene: status and prospects. *Science*, 324:1530–1534, 2009.

[4] C. H. Lui, L. Liu, K. F. Mak, G. W. Flynn, and T. F. Heinz. Ultraflat graphene. *Nature*, 462(7271):339–341, 2009.

[5] I. Ovid'Ko. Mechanical properties of graphene. *Rev. Adv. Mater. Sci*, 34(1):1–11, 2013.

[6] D. G. Papageorgiou, I. A. Kinloch, and R. J. Young. Mechanical properties of graphene and graphene-based nanocomposites. *Prog. materials science*, 90:75–127, 2017.

[7] E. P. Randviir, D. A. Brownson, and C. E. Banks. A decade of graphene research: production, applications and outlook. *Mater. Today*, 17(9):426–432, 2014.

[8] Z. Zhen and H. Zhu. Structure and properties of graphene. *Graphene*, pages 1–12, 2018.

[9] F. Mohd and M. Talha. Effect of graphene platelets reinforcement on vibration behavior of functionally graded porous arches under thermal environment. *Mater. Today: Proc.*, 61:103–109, 2022.

[10] M. Zanjanchi, M. Ghadiri, and S. Sabouri-Ghomi. Dynamic stability and bifurcation point analysis of fg porous core sandwich plate reinforced with graphene platelet. *Acta Mech.*, 234(10):5015–5037,, 2023.

[11] Y. Zhang, X. Guo, Z. Ni, Y. Zhang, H. Zhang, C. Lü, and J. Yang. Nonlinear frequency analysis of piezoelectric functionally graded porous plates reinforced by graphene platelets under thermo-electro-mechanical loads. *Mech. Adv. Mater. Struct.*, pages 1–17, 2025.

[12] D. Singh, R. Kiran, and R. Vaish. Vibration and buckling analysis of agglomerated cnt composite plates via isogeometric analysis using non-polynomial shear deformation theory. *Eur. J. Mech.*, 98:104892, 2023.

[13] R. Kiran, N. Nguyen-Thanh, J. Huang, and K. Zhou. Buckling analysis of cracked orthotropic 3d plates and shells via an isogeometric-reproducing kernel particle method. *Theor. Appl. Fract. Mech.*, 114:102993, 2021.

[14] F. Mohd and M. Talha. The influence of temperature variations on large-amplitude vibration of functionally graded metallic foam arches reinforced with graphene platelets. *Acta Mech.*, 234(2):425–450, 2023.

[15] C. Tao and T. Dai. Isogeometric analysis for postbuckling of sandwich cylindrical shell panels with graphene platelet reinforced functionally graded porous core. *Compos. Struct.*, 260:113258, 2021.

[16] Z. Li, J. Zheng, and Z. Zhang. Mechanics of the confined functionally graded porous arch reinforced by graphene platelets. *Eng. Struct.*, 201:109817, 2019.

[17] M. Khayat, A. Baghlani, S. M. Dehghan, and M. A. Najafgholipour. The influence of graphene platelet with different dispersions on the vibrational behavior of nanocomposite truncated conical shells. *Steel Compos. Struct.*, 38(1):47–66, 2021.

[18] J. Lu, Q. Yang, Z. Meng, K. Yang, W. Xu, and C. V. Chiu. Modeling and dynamic analysis of functionally graded porous spherical shell based on Chebyshev–Ritz approach. *Sci. Eng. Compos. Mater.*, 30(1):20220214, 2023.

[19] G. Wei and V. Tahouneh. Temperature dependent buckling analysis of graded porous plate reinforced with graphene platelets. *Steel Compos. Struct.*, 39(3):275–290, 2021.

[20] C. Ye and Y. Q. Wang. Nonlinear forced vibration of functionally graded graphene platelet-reinforced metal foam cylindrical shells: internal resonances. *Nonlinear Dyn.*, 1(3):2051–2069, 2021.

[21] L.-L. Zhang, L.-C. Zhao, S.-J. Lang, and K. Asemi. Free vibration analysis of functionally graded graphene platelet-reinforced metal foam doubly curved panel. *Front. Mater.*, 11:1339865, 2024.

[22] J.-P. Song and G.-L. She. Nonlinear resonance and chaotic dynamic of rotating graphene platelets reinforced metal foams plates in thermal environment. *Arch. Civ. Mech. Eng.*, 24(1):45, 2024.

[23] M. W. Teng and Y. Q. Wang. Nonlinear forced vibration of simply supported functionally graded porous nanocomposite thin plates reinforced with graphene platelets. *Thin-Walled Struct.*, 164:107799, 2021.

[24] H.-G. Pan, Y.-S. Wu, J.-N. Zhou, Y.-M. Fu, X. Liang, and T.-Y. Zhao. Free vibration analysis of a graphene-reinforced porous composite plate with different boundary conditions. *Materials*, 14(14):3879, 2021.

[25] J.-R. Cho. Free vibration analysis of functionally graded porous cylindrical panels reinforced with graphene platelets. *Nanomaterials*, 13(9):1441, 2023.

[26] L. Gu. Moving kriging interpolation and element-free galerkin method. *Int. journal for numerical methods engineering*, 56(1):1–11, 2003.

[27] C. H. Thai, T. N. Nguyen, T. Rabczuk, and H. Nguyen-Xuan. An improved moving kriging meshfree method for plate analysis using a refined plate theory. *Comput. & Struct.*, 176:34–49, 2016.

[28] T. Q. Bui and C. Zhang. Moving kriging interpolation-based meshfree method for dynamic analysis of structures. *Proc. Appl. Math. Mech.*, 11:197–198, 2011.

[29] L. Peng, S. Chen, W. Chen, and X. He. A moving kriging interpolation meshless for bending and free vibration analysis of the stiffened fgm plates in thermal environment. *Int. J. Comput. Methods*, 20(10):2350015, 2023.

[30] P. Hung, C. H. Thai, and P. Phung-Van. A moving kriging meshfree vibration analysis of functionally graded porous magneto-electro-elastic plates reinforced with graphene platelets. *Adv. Eng. Softw.*, 20(3):103885, 2025.

[31] T. Q. Bui and M. N. Nguyen. A moving kriging interpolation-based meshfree method for free vibration analysis of kirchhoff plates. *Comput. & structures*, 89(3-4):380–394, 2011.

[32] C. H. Thai, V. N. Do, and H. Nguyen-Xuan. An improved moving kriging-based meshfree method for static, dynamic and buckling analyses of functionally graded isotropic and sandwich plates. *Eng. Anal. with Bound. Elem.*, 64:122–136, 2016.

[33] J. Yang, D. Chen, and S. Kitipornchai. Buckling and free vibration analyses of functionally graded graphene reinforced porous nanocomposite plates based on Chebyshev-Ritz method. *Compos. Struct.*, 193:281–294, 2018.

[34] J. Choi and R. Lakes. Analysis of elastic modulus of conventional foams and of re-entrant foam materials with a negative poisson's ratio. *Int. J. Mech. Sci.*, 37(1):51–59, 1995.

[35] I. Gibson and M. F. Ashby. The mechanics of three-dimensional cellular materials. *Proc. royal society London. A. Math. physical sciences*, 382(1782):43–59, 1982.

[36] J. H. Affdl and J. Kardos. The halpin-tsai equations: a review. *Polym. Eng. & Sci.*, 16(5):344–352, 1976.

[37] R. G. De Villoria and A. Miravete. Mechanical model to evaluate the effect of the dispersion in nanocomposites. *Acta Materialia*, 55(9):3025–3031, 2007.

[38] C. H. Thai, A. Ferreira, and P. Phung-Van. A nonlocal strain gradient isogeometric model for free vibration and bending analyses of functionally graded plates. *Compos. Struct.*, 251:112634, 2020.

[39] C. H. Thai, A. Ferreira, and H. Nguyen-Xuan. Naturally stabilized nodal integration meshfree formulations for analysis of laminated composite and sandwich plates. *Compos. Struct.*, 178:260–276, 2017.

[40] Y. Du, S. Wang, L. Sun, and Y. Shan. Free vibration of rectangular plates with porosity distributions under complex boundary constraints. *Shock. Vib.*, 2019(1):6407174, 2019.

[41] M. A. Rafiee, J. Rafiee, Z. Wang, H. Song, Z.-Z. Yu, and N. Koratkar. Enhanced mechanical properties of nanocomposites at low graphene content. *ACS nano*, 3(12):3884–3890, 2009.

[42] M. Song, S. Kitipornchai, and J. Yang. Free and forced vibrations of functionally graded polymer composite plates reinforced with graphene nanoplatelets. *Compos. Struct.*, 159:579–588, 2017.

[43] M. Arefi, E. M.-R. Bidgoli, R. Dimitri, and F. Tornabene. Free vibrations of functionally graded polymer composite nanoplates reinforced with graphene nanoplatelets. *Aerosp. Sci. Technol.*, 81:108–117, 2018.

[44] R. M. R. Reddy, W. Karunasena, and W. Lokuge. Free vibration of functionally graded-gpl reinforced composite plates with different boundary conditions. *Aerosp. Sci. Technol.*, 78:147–156, 2018.

[45] C. H. Thai, A. Ferreira, and P. Phung-Van. Size dependent free vibration analysis of multilayer functionally graded gplrc microplates based on modified strain gradient theory. *Compos. Part B: Eng.*, 169:74–188, 2019.

About Authors

Le Thanh DAT was born in Vietnam in 2003. He is currently a final-year student at Ho Chi Minh City University of Technology and Education. His major is mechanical engineering. This is his first time researching composite structures.

Pham Tan HUNG was born in Vietnam in 1981. He has a Ph.D. degree in Mechanics. Now, he is a lecturer at the Faculty of Civil Engineering at Ho Chi Minh City University of Technology and Education, Ho Chi Minh City, Vietnam. His research interests are the computational mechanics.

